Journal of Biomechanics 97 (2019) 109370

Contents lists available at ScienceDirect

Journal of Biomechanics

journal homepage: www.elsevier.com/locate/jbiomech
www.JBiomech.com

Analyzing acoustoelastic effect of shear wave elastography data for perfused and hydrated soft tissues using a macromolecular network inspired model

D. Rosen, J. Jiang *

Department of Biomedical Engineering, Michigan Technological University, 1400 Townsend Drive, Houghton, MI, USA

ARTICLE INFO

Article history:
Accepted 22 September 2019

Keywords:
Shear wave elastography
Acoustoelasticity
Hydrated tissue

ABSTRACT

Shear wave elastography (SWE) has enhanced our ability to non-invasively make *in vivo* measurements of tissue elastic properties of animal and human tissues. Recently, researchers have taken advantages of acoustoelasticity in SWE to extract nonlinear elastic properties from soft biological tissues. However, most investigations of the acoustoelastic effects of SWE data (AE-SWE) rely on classic hyperelastic models for rubber-like (dry) materials. In this paper, we focus solely on understanding acoustoelasticity in soft hydrated tissues using SWE data and propose a straightforward approach to modeling the constitutive behavior of soft tissue that has a direct microstructural/macromolecular interpretation. Our approach incorporates two constitutive features relevant to biological tissues into AE-SWE: static dilation of the medium associated with nonstructural components (*e.g.* tissue hydration and perfusion) and finite extensibility derived from an ideal network of biological filaments. We evaluated the proposed method using data from an in-house tissue-mimicking phantom experiment, and *ex vivo* and *in vivo* AE-SWE data available in the SWE literature. In conclusion, predictions made by our approach agreed well with measurements obtained from phantom, *ex vivo* and *in vivo* tissue experiments.

1. Introduction

In the past decade, shear wave elastography (SWE) (Tanter et al., 2013) has emerged as a clinically useful medical imaging technique. Although the term SWE is typically associated with medical ultrasound (Tanter et al., 2013), elastographic techniques built around the same elastic wave mechanics have been implemented on magnetic resonance (Mariappan et al., 2010) and optical (Larin and Sampson, 2017) imaging systems to detect changes in tissue elasticity due to disease or functional state. As such SWE has been applied to estimate elasticity in soft tissue at the whole organ level down to the cellular level (Grasland-Mongrain et al., 2018) and its range of clinical applications span a variety of pathological conditions including liver fibrosis (Nightingale et al., 2015), neoplasms assessment (Correas et al., 2015), preterm birth (Carlson et al., 2015), and musculoskeletal applications (DeWall et al., 2014).

Because soft tissue is highly deformable and displays prominent nonlinear strain stiffening effects (Humphrey, 2003), substantial alterations of (group) shear wave speed (SWS) from tissue deformation are expected due to acoustoelasticity (AE). Such alterations are recognized as a source of user variation in SWE (Barr and Zhang, 2012) and have prompted recommendations to limit manual compression of tissue during SWE measurements in order to limit user dependency (Barr et al., 2015). Recently, coupling SWE measurement with a known deformation to measure the resulting AE effect—hereafter referred to as AE-SWE—has been adopted as a means of estimating nonlinear elastic parameters (Gennisson et al., 2007; Latorre-Ossa et al., 2012; Jiang et al., 2015; Jiang et al., 2015). The potential applications of characterizing nonlinear elasticity are being investigated in various organs or materials including breast lesions (Bernal et al., 2016), transplanted kidney (Aristizabal et al., 2018) and heel-pads (Chatzistergos et al., 2018). Estimation of these parameters requires the formulation of AE equations coupled with an appropriate hyperelastic strain energy function (Rosen and Jiang, 2019). However, most previous treatments of AE have relied on the same basic constitutive assumptions like that of hyperelasticity in dry rubbery materials: a single-phase solid medium that is volumetrically undeformable. In contrast, the solid phase of *in vivo* soft tissue is typically infiltrated by a fluid phase due to tissue perfusion and tissue hydration (*i.e.* fluid content within the cells and interstitial spaces). Changes in these fluid

* Corresponding author.
E-mail address: jjiang1@mtu.edu (J. Jiang).

https://doi.org/10.1016/j.jbiomech.2019.109370
0021-9290/

phases result in changes in both volume and elasticity of biological tissues (Helfenstein et al., 2015; Singh et al., 2018).

To our knowledge, only two previous approaches have been proposed for the analysis of SWE measurements that incorporate the effect of a fluid phase in their constitutive treatment: the micro-channel model proposed by Prof. Parker (Parker, 2014); and the poroelastic AE analysis proposed recently by Nazari and Prof. Barbone (Nazari et al., 2018). These formulations are targeted toward analyzing SWS values in relation to tissue perfusion and each has its relative advantages and limitations. Although the micro-channel model (Parker, 2014) can be used to relate frequency-dependent dispersion and quasi-static relaxation in biological tissues to the underlying microvasculature, its development relies on small-strain linear elasticity and AE is effectively neglected. For the aforementioned poroelastic AE analysis (Nazari et al., 2018), its main advantages are that it can be applied to large volume strains produced from changes in the fluid phase and momentum exchange between the fluid and solid phases are incorporated. However, currently, it has only been formulated for purely volumetric deformation and a constant perfusion pressure (*i.e.* no fluid flow and associated pressure drop). Applying their poro-acoustoelastic formulation in the case of the axial deformations considered in AE-SWE and the fluid flow expected for *in vivo* perfusion would involve complicated boundary conditions and additional quantities that are difficult to acquire simultaneously with SWE. It is also worth noting that neither approach incorporates tissue hydration as a component of the fluid phase in biological tissue.

In all of these previous approaches, a common downside to the hyperelastic strain energy functions used to model elastic nonlinearity is that they are strictly phenomenological. As a result, it is difficult to interpret their corresponding parameters relative to the underlying microstructural characteristics of the tissue. Adopting a strain energy function with parameters that can be interpreted relative to the underlying tissue microstructure would provide a clearer picture of how SWE and AE-SWE measurements relate to the disease or functional state of the biological tissue. For example, in the strain elastography literature where the characterization of elastic nonlinearity has been proposed for detection of a cancerous breast lesion, there has been much discussion of how elastic nonlinearity might relate to the tortuosity of collagen fibrils in benign and malignant lesions (Hall et al., 2011; Goenezen et al., 2012). This discussion has culminated into an initial analytic treatment relating these two characteristics (Liu et al., 2017).

In this work, we propose a constitutive model that is applicable to explain alterations among AE-SWE measurements associated with changes in the fluid phase of the hydrated medium. More specifically, drawing insights from the macromolecular modeling literature for swollen polymeric networks, the proposed approach incorporates two key features: (1) pure dilation of the elastic continuum coupled with additional deformation and (2) a strain energy function that incorporates elastic nonlinearity through finite extensibility. These features are illustrated in Fig. 1. More specifically, the overall deformation is split into dilational and isochoric stretches (Boyce and Arruda, 2001; Liu et al., 2015), where the dilational stretch is associated with the permeation of a solid network by a fluid phase, as illustrated in Fig. 1c. Simultaneously, the strain energy function adopted herein was originally derived for an idealized network of worm-like chains that possesses chain-limited extensibility (Dobrynin and Carrillo, 2011). Thus both of these features have macromolecular justifications/interpretations that are illustrated in Fig. 1c and d. In addition to formulations presented below, the proposed approach is applied to analyze data obtained from an in-house tissue-mimicking phantom experiment and *ex vivo* and *in vivo* SWE experiments reported in the literature.

2. Theory

We model hydrated and perfused soft tissues as a homogeneous and elastic dry network of worm-like chains permeated by both static and flowing fluid components. This results in an isotropic, bi-phasic media composed of nearly incompressible constituent phases. Instead of solving the momentum balance between the fluid and solid phases as in (Nazari et al., 2018), we limit the acoustoelastic analysis to the strain energy of the elastic phase. Furthermore, the strain energy only increases when an external traction/force or internal pressure does work on it through deformation.

2.1. Multiplicative decomposition of isometric dilation and isochoric deformation

The reference configuration of the elastic phase (*i.e.* the datum for zero strain energy) is set to its dry, undiluted state and the deformation experienced by the elastic network is assumed to be quasi-static. In such a case, the deformation tensor, F, can be decomposed into an isometric dilation F_d and an isochoric deformation $\tilde{F}$ as follows

$$F = \begin{bmatrix} \lambda_1 & 0 & 0 \\ 0 & \lambda_2 & 0 \\ 0 & 0 & \lambda_3 \end{bmatrix} = F_d \tilde{F} = \begin{bmatrix} \Lambda & 0 & 0 \\ 0 & \Lambda & 0 \\ 0 & 0 & \Lambda \end{bmatrix} \begin{bmatrix} \tilde{\lambda}_1 & 0 & 0 \\ 0 & \tilde{\lambda}_2 & 0 \\ 0 & 0 & \tilde{\lambda}_3 \end{bmatrix} \tag{1}$$

where Λ denote the stretch due to pure (isotropic) dilation (F_d) and $\tilde{\lambda}_1, \tilde{\lambda}_2$, and $\tilde{\lambda}_3$ the three principle stretches of $\tilde{F}$, respectively (hereafter, associated quantities for $\tilde{F}$ will be denoted with a tilde). Because $\tilde{F}$ is isochoric, its determinant is unity (*i.e.* $det\left(\tilde{F}\right) = 1$). The Jacobian, J of F can then be expressed in terms of the volume fraction of the ideal network ϕ as follows (Boyce and Arruda, 2001),

$$J = det(F) = det(F_d) det\left(\tilde{F}\right) = \Lambda^3 = 1/\phi \tag{2}$$

For a plane shear wave with propagation and polarization directions in line with the principle axis of λ_2 and λ_1, respectively, Ogden derived the following acoustoelastic expression (Ogden, 2007),

$$\rho v^2 = A_{02121} = J^{-1} \lambda_2^2 \frac{\lambda_1 \frac{\partial W}{\partial \lambda_1} - \lambda_2 \frac{\partial W}{\partial \lambda_2}}{\lambda_1^2 - \lambda_2^2} \tag{3}$$

where ρ denotes the mass density, v denotes the shear wave speed (SWS), A_{02121} is a component of the elasticity tensor in the deformed reference frame, and W is the strain energy function of the ideal network. For an isotropic strain energy function defined in terms of the invariants I_1, I_2 and I_3 of the Cauchy-Green deformation tensor $C = F^T F$, Eq. (3) can be developed (see Supplementary Materials for detailed derivation) into the following expression:

$$\rho v^2 = J^{-1} \left(2\lambda_2^2 \frac{\partial W}{\partial I_1} + 2\lambda_2^2 \lambda_3^2 \frac{\partial W}{\partial I_2} \right) = 2 \frac{\tilde{\lambda}_2^{\,2}}{\Lambda} \frac{\partial W}{\partial I_1} + 2\Lambda \tilde{\lambda}_1^{-2} \frac{\partial W}{\partial I_2} \tag{4}$$

Note that when $\tilde{F} = I$, Eq. (4) is identical to the dry-phase shear modulus proposed by Nazari and Barbone (Nazari et al., 2018). Likewise, when $\Lambda = 1$, Eq. (4) is in agreement with our early work for an incompressible solid (Rosen and Jiang, 2019).

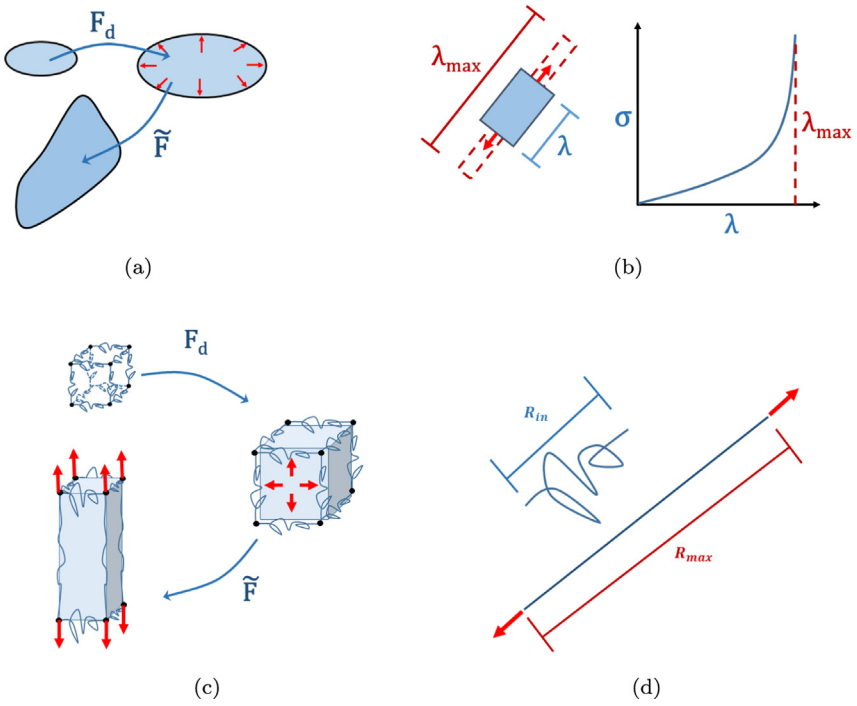

Fig. 1. Diagramatic representations the dilation/isochoric decomposition of deformation (1a) and of finite extensibility in material elasticity (1b). The macromolecular interpretation of (1a) is illustrated in (1c) of an a network of chains/filaments that are permeated by a fluid phase that moves with the network under stretching. Finite extensiblity can be interpreted as straightening of the network chains/filaments (1d).

2.2. Strain energy function incorporating chain-limited extensibility

In order to proceed, an explicit form for the strain energy function W is required. We adopted a constitutive model first proposed by Dobrynin et al. (Dobrynin et al., 2010). The model was derived to incorporate the features of a network of worm-like chains and has been demonstrated on hydrogels of biological filaments and dry polymeric networks (e.g. dry rubber) (Dobrynin and Carrillo, 2011). Its strain energy function has the following form

$$W = \frac{\mu_N}{3}\left(I_1 - 3 - \frac{6}{\beta(\beta I_1/3 - 1)} + \frac{6}{\beta(\beta - 1)}\right) \tag{5}$$

where μ_N is the so called network shear modulus and β is the non-linearity parameter that defines the maximum finite stretch of the medium. In terms of the network interpretation of Eq. (5) illustrated in Fig. 1d, β is approximately the mean squared ratio of the intrinsic length of the coiled network chains R_{in} and to their uncoiled length R_{max} (i.e. $\beta \approx \langle R_{in}\rangle / R_{max}$). A detailed discussion of the physical underpinnings of the parameters μ_N and β can be found elsewhere (Dobrynin et al., 2010; Dobrynin and Carrillo, 2011).

Substituting Eq. (5) into Eq. (4) and replacing Λ with $J^{1/3}$ produces

$$\rho v^2 = \tilde{\lambda}_2^2 J^{-1/3}\frac{\mu_N}{3}\left(1 + \frac{2}{\left(1 - \beta J^{2/3}\tilde{I}_1/3\right)^2}\right) \tag{6}$$

Note that when $F = I$, Eq. (6) produces $\rho v^2 = \mu_N / 3\left(1 + 2(1-\beta)^{-2}\right)$ which reduces to $\rho v^2 = \mu_N$ where $\beta \approx 0$. Because the reference configuration is set to the undilated (*i.e.* dry) state of the elastic solid, knowledge of the absolute dilation is required for Eq. (6), which may or may not be available. Here we propose decomposing J in Eq. (6) into an initial, potentially unknown, static dilation J_0 and any additional quasi-static dilation, $\hat{J}$ through $J = J_0\hat{J}$. This multiplicative decomposition is viable due to the properties of the determinant operator that defines J. Eq. (6) can then be adjusted to

$$\rho v^2 = \tilde{\lambda}_2^2 \hat{J}^{-1/3}\frac{\hat{\mu}_N}{3}\left(1 + \frac{2}{\left(1 - \hat{\beta}\hat{J}^{2/3}\tilde{I}_1/3\right)^2}\right) \tag{7}$$

where $\hat{\mu}_N$ and $\hat{\beta}$ are regarded as effective parameters of μ_N and β. They are defined as

$$\hat{\mu}_N = J_0^{-1/3}\mu_N, \quad \hat{\beta} = J_0^{2/3}\beta \tag{8}$$

Also, in Eq. (7), $\tilde{I}_1 = \tilde{\lambda}_1^2 + \tilde{\lambda}_2^2 + \tilde{\lambda}_3^2$ (see Eq. (1)).

Alternatively, an assumed value for J_0 can be arrived at with knowledge of the composition of the medium. For instance, where the volume fraction of the elastic medium is known, Eq. (2) can be applied. However, it is more frequent for compositional information to be reported as mass fractions. If the density of the structural (worm-like chain) ρ_s and non-structural (fluid), ρ_{ns} components are known, then J_0 can be inferred from mass fraction of the structural phase p_s as follows

$$J_0 = \frac{1}{\phi} = \frac{V_s + V_{ns}}{V_{ns}} = 1 + \rho_s/\rho_{ns}(1/p_s - 1) \tag{9}$$

It is important to note that Eq. (7) can be used to analyze AE-SWE measurements for bio-materials with or without volumetric dilations. If a medium being imaged is under external mechanical loading, it will be assumed that the overall deformation applied to the medium is isochoric (*i.e.* $\hat{J} = 1$ and $\tilde{\lambda}_2 \neq 1$, $\tilde{I}_1 \neq 1$ that should be evaluated for each loading step.) Then, Eq. (7) can be used for AE analyses similar to those already reported in the literature (Jiang et al., 2015; Jiang et al., 2015; Rosen and Jiang, 2019). If there is non-zero net fluid flow into the medium, $\hat{J}$ can be evaluated through $\hat{J} = J/J_0$ to reflect the volume changes, while the

$\tilde{\lambda}_2 = 1$, $\tilde{I}_1 = 1$ in Eq. (7) in the absense of external loading. Consequently, how the changes in the net fluid flow (*e.g.* due to perfusion) influence the SWS can be modeled.

3. Methods and materials

3.1. Swollen phantom experiment

A hydrogel swelling experiment was conducted on a cylindrical elastography phantom used in a previous AE-SWE experiment (Rosen and Jiang, 2019). The phantom was composed of 10% gelatin and 3% sigma-cell (Sigma-Aldrich Inc., MI, USA) by weight. Formaldehyde was also incorporated into the gelatin solution prior to congealing (0.047 grams of per gram dry weight gelatin). This introduced stable chemical crosslinks into the gelatin network in addition to the physical cross-links that form due to the concentration of gelatin. J_0 was calculated using Eq. (2) and assuming a density of 1.35 g/ml for gelatin (Fischer et al., 2004) and 1 g/mL for the water.

The experiment was conducted as follows. First, an initial AE-SWE measurement was collected. The AE-SWE measurements followed the methodology laid out in Rosen and Jiang (2019) for a top orientation of the transducer. Briefly, measurements were collected by placing the phantom between a lab jack and a stationary acrylic plate with an opening for the ultrasound transducer (see Fig. 2a and b). Compression was applied by adjusting the height of the lab jack and a caliper was used to measure the compression applied to the phantom. SWE measurements were collected at different compression levels during 3 separate compression cycles and the phantom was unloaded after each compression cycle. SWE measurements were collected using a linear array transducer (L7-4, ATL, Phillips Inc., WA, USA) connected to a research ultrasound system (V1 system, Verasonics Inc., WA, USA). A point shear wave elastography (Shiina et al., 2015) sequence was programmed for these measurements: A single pushing pulse induced shear waves and SWS was estimated from the resulting shear wave data using the Fourier-domain shift matching (FDSM) method (Rosen and Jiang, 2018). Particularly, the FDSM method estimated SWS over a small region (5 mm [axial] by 10 mm [lateral]) lateral to the pushing pulse. Technical details of the SWE acquisition process has been previously reported in detail in (Rosen and Jiang, 2018). After the initial AE-SWE measurement, the phantom was fully submersed in a deionized water bath for approximately 18 days. As this polymeric swelling is a diffusion process, the spatial variation of SWE measurements from the swollen phantom was checked at approximately 15 days. No spatial trend was observed (see the supplementary materials for details). The phantom was occasionally removed from the water bath and weighed. The weight change of the phantom was used to recalculate J_0 using Eq. (9) as shown in Fig. 2c. This was done to monitor the time course of swelling. After swelling, the AE-SWE measurements were repeated. These

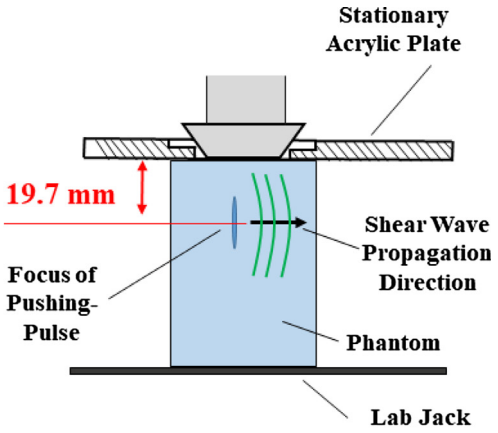

(a)

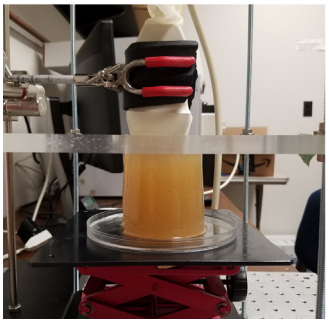

(b)

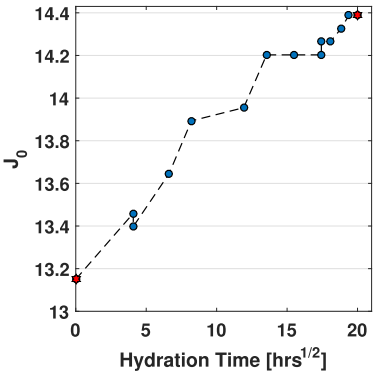

(c)

Fig. 2. Diagramatic (2a) and photographic representations (2b) of experimental setup for in-house AE-SWE measurements. SWE measurements were collected from the top of the phantom while manual adjustment of a lab jack was used to apply quasi-static deformation. A stationary acrylic plate with an opening for the transducer was used maintain uniaxial deformation. The time-course of volumetric deformation of the phantom (2c) during the swelling process suggests Fickian diffusion (i.e. is linearly proportional to the square root of time). The red hexagonal markers denote the beginning and endpoitns at which AE-SWE measurements were collected.

measurement were analyzed assuming uniaxial deformation (*i.e.* $\tilde{\lambda}_1 = \lambda, \tilde{\lambda}_2 = \tilde{\lambda}_3 = \lambda^{-1/2}$).

3.2. Reanalysis of ex vivo and in vivo AE-SWE experiments

In order to investigate the applicability of the proposed theory to biological tissues, SWE and AE-SWE experiments reported in the literature for *ex vivo* porcine tissue were re-analyzed using the framework described in Section 2. Experiments on porcine tissues were selected because chemical analysis of *ex vivo* tissue composition of each organ is available in the literature (Babicz et al., 2018). For the purpose of this study, it was assumed that the structural phase is composed exclusively of protein and that the concentration of non-structural protein was negligible. As such, assuming a density of 1.35 g/mL for protein (Fischer et al., 2004) and 1 g/mL for the fluid phase (*i.e.* the mass density of water), the volume fraction of the structural phase could be calculated using Eq. (9). AE-SWE measurements reported in the literature for fresh *ex vivo* porcine liver (Jiang et al., 2015; Vachutka et al., 2018) were collected and reanalyzed using the proposed framework. Principle stretches were parameterized as was done in Jiang et al. (2015), *i.e.*, $\tilde{\lambda}_1 = \lambda, \tilde{\lambda}_2 = \lambda^{-\xi}$, $\tilde{\lambda}_3 = \lambda^{1-\xi}$. As reported in (Jiang et al., 2015 and Jiang et al., 2015), ξ was taken to be equal to 0.1.

As a preliminary application of the proposed theory to *in vivo* human tissue, SWE measurements of compressed human breast tissues (Barr and Zhang, 2012; Jiang et al., 2015) were re-analyzed. As with the *ex vivo* porcine tissue data, the axial deformation produced by the transducer compression was parameterized, using the parameterization reported in Jiang et al. (2015) of $\xi = 0.1$. The volume fraction of the dry network was derived from the averages of mass percentages reported in Woodard and White (1986) under the same assumptions used in the *ex vivo* porcine tissue. The weight percentage of protein from Woodard and White (1986) was 4.433%.

3.3. Perfusion pressure experiments on porcine kidney cortex

As a case study of the significance of incorporating dilation deformation into our analysis of SWE, we also applied our analysis to the perfusion pressure experiments reported by Helfenstein et al. (Helfenstein et al., 2015) on *ex vivo* porcine kidneys. The data from this kidney experiment was selected because, in contrast to experiments such as the canine study (Rotemberg et al., 2011), data associated with the volumetric change of the tissue due to the pressure applied to perfuse the tissue was available in this experiment through measurements of organ dimensions. Additional data from an analogous *in vivo* experiment that included magnetic resonance imaging-based volume measurements of the kidney during vascular occlusion (Warner et al., 2011) were available for comparison.

3.4. Data analysis

Material parameters were estimated through constrained nonlinear least-squares regression (*i.e.* lsqnonlin function), which was implemented using the Optimization Toolbox in MATLAB (Version 2016a, Mathworks,Inc, MA, USA). Curve fitting was applied to Eq. (7), where $\hat{\mu_N}$ and $\hat{\beta}$ are the parameters being estimated. The regression coefficients were constrained to $0 < \hat{\mu}_N < \infty$ and $0 < \hat{\beta} < 3/\max\left\{\widetilde{\hat{J}I}_1\right\}$, where $\max\left\{\widetilde{\hat{J}I}_1\right\}$ denotes the maximum value of $\widetilde{\hat{J}I}_1$ for the given dataset. Incorporating this dataset specific constraint prevented misfitting to local minima associated with non-physical parameter estimates (see supplementary material for details). The initial guesses used for the coefficients of the nonlinear regression were set to $\hat{\mu}_N = \rho v_0^2$ and $\hat{\beta} = 0$, which corresponds to a infinitely extensible network of worm-like chains (Dobrynin and Carrillo, 2011). The effective parameters were converted to their absolute counterparts using Eq. (8).

4. Results

The combined results for the parameter estimation for all experiments considered are reported in Table 1, including the proposed effective parameters and 95% confidence intervals for parameter estimates. The numbering for each set of parameter fits in Table 1 will be used consistently to denote the plotted curves in Figs. 3–6. Note that the resulting curve fits produce very high R^2 values ($0.970 \sim 0.998$) for all fitted curves.

Referring to the swollen phantom experiment, the changes in absolute swollen volume, calculated from changes in the phantom mass using Eq. (2), suggest a Fickian diffusion process: Changes are linearly proportional to the square of time (see Fig. 2c). Fig. 3

Table 1
Fitted parameters for all data reported. Values in parenthesis denote the upper and lower bounds of the confidence intervals associated with the parameter estimation (%95 confidence range).

Dataset #	Medium	Data Source	$\hat{\mu_N}$	$\hat{\beta}$	R^2	μ_N	β	J_0
1	Gelatin Phantom (initial)	in-house (Rosen and Jiang, 2019)	3.191 (3.033, 3.350)	0.447 (0.4354, 0.459)	0.992	7.533 (7.159,7.907)	0.080 (0.078, 0.082)	13.15
2	Gelatin Phantom (Swollen)	in-house (Rosen and Jiang, 2019)	1.868 (1.784, 1.953)	0.528 (0.520, 0.537)	0.993	4.544 (4.338, 4.750)	0.089 (0.088, 0.091)	14.38
3	Pig Liver (1)	(Jiang et al., 2015)	0.306 (0.262, 0.351)	0.766 (0.757. 0.775)	0.993	0.523 (0.448, 0.599)	0.263 (0.259,0.266)	4.98
4	Pig Liver (2)	(Jiang et al., 2015)	0.257 (0.175,0.339)	0.766 (0.757,0.775)	0.970	0.493 (0.298, 0.580)	0.269 (0.263, 0.275)	4.98
5	Pig Liver (3)	(Jiang et al., 2015)	0.099 (0.080, 0.118)	0.863 (0.855, 0.871)	0.994	0.169 (0.136, 0.201)	0.296 (0.293. 0.299)	4.98
6	Pig Liver (4)	(Vachutka et al., 2018)	0.075 (0.036, 0.113)	0.924 (0.913, 0.934)	0.983	0.128 (0.062,0.194)	0.317 (0.313, 0.320)	4.98
7	Glandular Tissue (1)	(Barr and Zhang, 2012)	0.409 (0.343, 0.476)	0.693 (0.687, 0.700)	0.996	0.797 (0.668, 0.927)	0.182 (0.181, 0.184)	7.409
8	Glandular Tissue (2)	(Jiang et al., 2015)	0.440 (0.317,0.563)	0.673 (0.667, 0.679)	0.998	0.858 (0.619, 1.098)	0.177 (0.175, 0.179)	7.409
9	Pig Kidney Cortex	(Helfenstein et al., 2015)	1.279 (0.643, 1.915)	0.566 (0.524, 0.608)	0.991	2.540 (1.277, 3.803)	0.144 (0.133, 0.154)	7.832

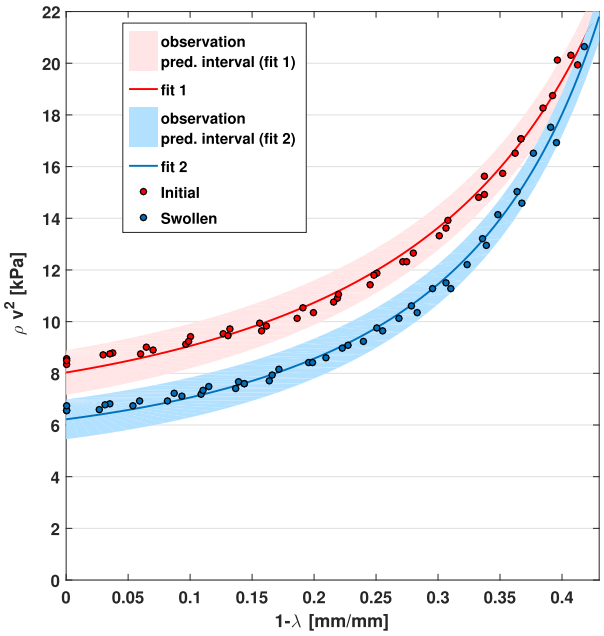

Fig. 3. The vertical axis is SWS derived shear modulus (ρv^2). The horizontal axis corresponds to degree of compression (parameterized by $1-\lambda$). The AE-SWE measurements taken before and after swelling suggest that alterations in the polymeric network manifest in alterations in $\hat{\mu}_N$ and $\hat{\beta}$.

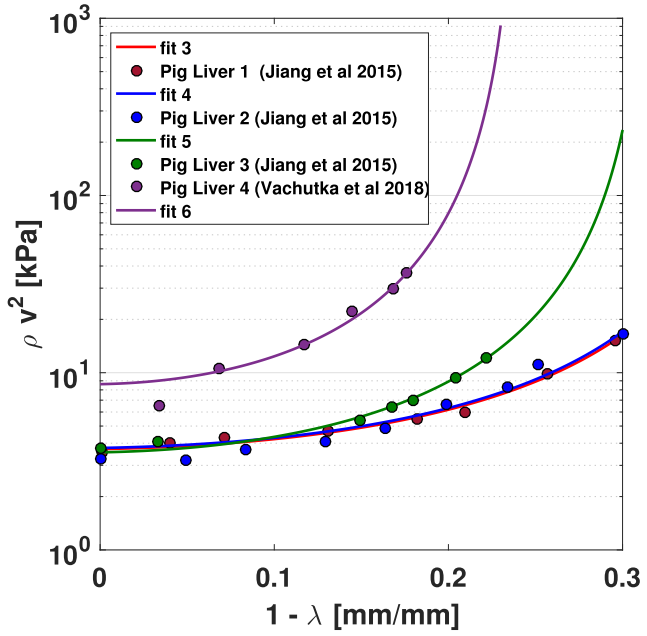

(a)

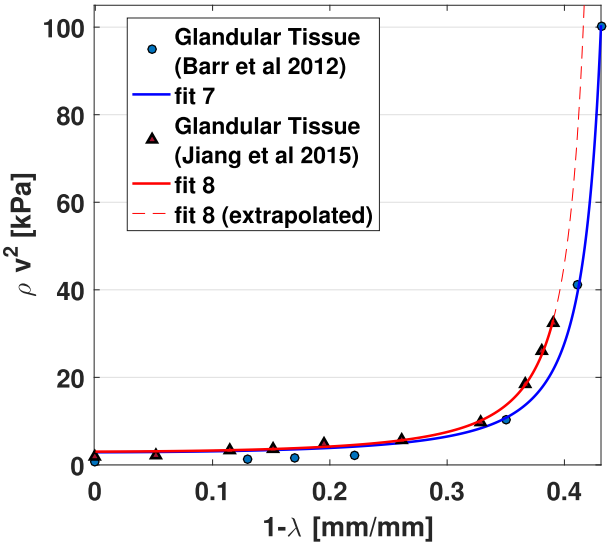

(b)

Fig. 4. AE-SWE experiments for ex vivo pig liver (4a) and *in vivo* glandular tissue of the human breast (4b). The vertical axis is SWS derived shear modulus (ρv^2). The horizontal axis corresponds to degree of compression (parameterized by $1-\lambda$). The vertical axes in (4a) is logarithmically scaled in order accommodate the wide range of values.

shows the changes in SWE measurements after swelling along with the associated curve fit and associated observation prediction intervals at 95% confidence.

Fig. 4 displays fitted curves and corresponding data from reanalysis of AE-SWE measurements reported for *ex vivo* pig liver (see Fig. 4a) and *in vivo* glandular tissue of the human breast (Fig. 4b). In the case of the *ex vivo* pig liver measurements, large variation in AE-SWE measurements can be observed.

Fig. 5 displays the resulting analysis of perfusion pressure induced volumetric dilation on SWE measurements of the porcine kidney. Note that although the fitted curve (fit 8; See Table 1) was estimated exclusively from measurements on the artificially perfused *ex vivo* porcine kidney in (Helfenstein et al., 2015), analogous measurements for physiologically perfused and unperfused *in vivo* pig kidney are in excellent agreement with the resulting curve. Likewise, aggregated means from SWE measurements of *in vivo* and (fresh; never frozen) *ex vivo* measurements displayed in the marginal plots appear to align with the portions in the curve associated with un-perfused and physiologically perfused measurements, respectively. In contrast, measurements on *ex vivo* kidneys that were previously frozen and thawed before measurement, do not fall along the plot at all, suggesting a distinct change in material constitution due to the freeze-thaw process.

Fig. 6 illustrates the effect of incorporating static dilation J_0 using Eq. (8). Parameters reported in Table 1 are plotted together with parameters reported for hydrogels composed of biological filaments and for dry rubber (Dobrynin and Carrillo, 2011). It is generally observed from Fig. 6 that incorporation of J_0 produces an increase μ_N and a decrease in β. Additionally, while $\hat{\beta}$ for the various tissue were similar to parameters reported for hydrogels composed of biological filaments, after incorporating J_0 into the estimation, there was a general trend toward similarity with parameters reported for dry, natural rubber.

5. Discussion and conclusion

The strong agreement found between the model fits produced in our approach and both AE-SWE data and SWE data from perfusion pressure experiments (see Table 1 and associated curves in Figs. 3–5) suggests that it is a viable approach to modeling AE in fluid permeated elastic media. The results presented in Fig. 6 suggest that the effect of the volumetric dilation associated with network permeation by a fluid phase is a substantial increase in elastic nonlinearity. From the proposed macromolecular interpretation, this is a result of stretching the filamentous network structures of the tissue to near their maximum length. Results from the phantom experiment are especially suggestive in this respect, as a substantial increase in the rate of strain stiffening was observed in both the AE-SWE data (Fig. 3) and the estimates of $\hat{\beta}$ (Table 1). This

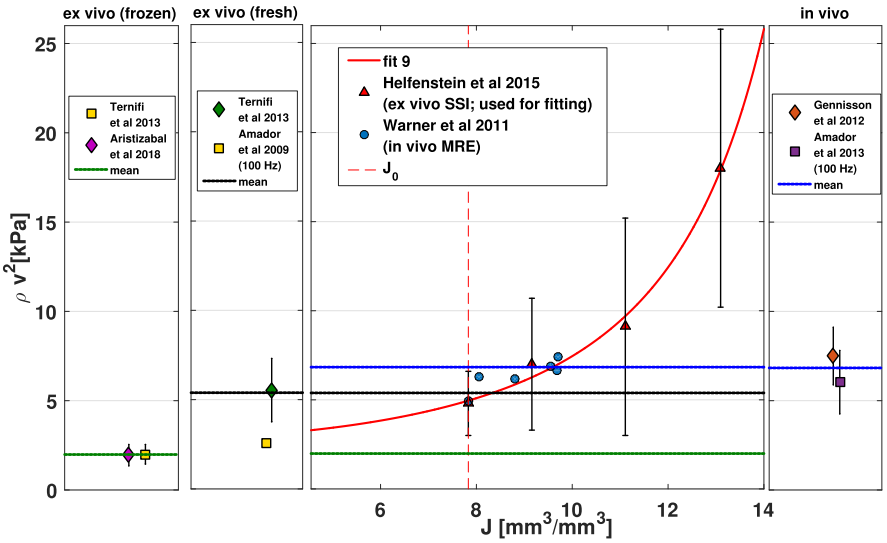

Fig. 5. SWS derived shear modulus (ρv^2) as a function of absolute volumetric deformation ($J = J_0\hat{J}$) for porcine kidney cortex (center plot). Fitting was applied data reported for SWE measurements using an ultrasonic technique (SuperSonic Shear Wave Imaging) of *ex vivo* porcine kidneys (red triangles). *In vivo* SWE measurements from magnetic resonance imaging (blue markers) are also plotted for comparison. Horizontal lines display the means of aggregated results (weighted by number of kidneys in experiment) from *ex vivo* (Amador et al., 2009; Ternifi et al., 2013; Aristizabal et al., 2018) (left margin) and *in vivo* (Gennisson et al., 2012; Amador et al., 2013) (right margin.) experiments..

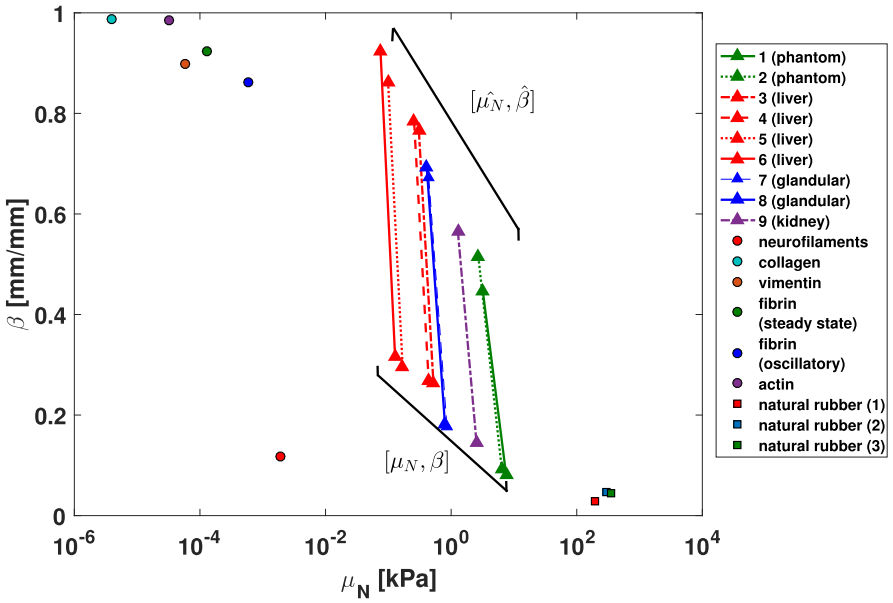

Fig. 6. Combined plot of parameters from all data fits. The data fits labeled based on their number in Table 1 and common line colors correspond to common mediums (i.e. red for liver, blue for breast tissue, etc.) The end points of each line (△) correspond to the sets of parameters $\hat{\mu}, \hat{\beta}$ and μ, β. For comparison, parameter estimates from (Dobrynin et al., 2010) for biological networks (○) and dry rubber (□) are also plotted. The horizontal axis is logarithmically scaled to accommodate the wide range of μ_N.

effect was substantially attenuated after factoring the initial dilation state of the elastic network. Results from the *in vivo* and *ex vivo* tissues only circumstantially support this assertion. However, the possibility becomes more interesting when considering other observations from the tissue characterization literature. Particularly, results from optical and magnetic resonance-based tissue characterization of *in vivo* breast lesions suggests that malignant breast lesions tend to have a higher water content then benign lesions (Shah et al., 2006; Haddadin et al., 2009; Chung et al., 2008; Evers et al., 2011). This, combined with the observation that elastographic measurements also showed elevated nonlinearity in malignant breast lesions (Goenezen et al., 2012) is in line with the theory from our approach. This should offer strong motivation for investigators to consider elastic nonlinearity when targeting the biomechanics of a functional or disease state of tissue accompanied by a change in fluid composition. In the future, a multimodal approach that couples a modality sensitive to tissue composition with AE-SWE measurement may prove insightful when interpreted through the proposed theory.

Given that there are many different types of biological tissues and various physiological conditions, there is ample room for different approaches. Our approach has several important practical and theoretical distinctions from the previously described alternatives. Practically, its main advantage is that the quantities required for its application are SWE and deformation measurements, which can often be attained *in vivo* through imaging. Theoretically, our

approach treats AE in a strictly kinematic and energetic sense (*i.e.* its formulated from relationships between strain energy and deformation and the internal stresses/pressure within the elastic medium or solid-fluid interfaces are not explicitly solved.) As such, it is not yet formulated such that it could relate SWE to kinetic quantities such as pressure, as was done in Nazari et al. (2018).

It should be noted that our work is within the framework of hyperelasticity. As such, incorporating the influence of the fluid phase on shear wave propagation beyond the added strain energy (see Eq. (2.2)) is not straightforward. Thus, dissipative effects such as poroelastic/viscoelastic relaxation and wave-dependent dispersion are not captured as in alternative analyses (*i.e.* (Nazari et al., 2018; Parker et al., 2016)). We consider this as a limitation of our current approach. Our future plan includes refinements of the theory by considering how these dissipative factors may affect acoustoelasticity of soft tissues.

In this study, we investigated a novel and straightforward approach to incorporating fluid permeation into AE analysis of SWE. To our knowledge, this is the first analysis applied to modeling both AE-SWE measurements and SWE alterations associated with varied perfusion pressure. Our approach suggests these effects are connected through elastic nonlinearity, which we modeled using a macromolecular-derived strain energy function.

Declaration of Competing Interest

None.

Acknowledgments

The project was funded by grants from US National Institutes of Health/National Institute of Biomedical Imaging and Bioengineering (R15-EB026197), a Portage Health Foundation Research Assistantship, and a Finishing Fellowship from Michigan Technological University. The authors thank Ms. Lydia Kugler from Michigan Technological University for assistance in compiling the literature in Fig. 5.

Appendix A. Supplementary material

Supplementary data associated with this article can be found, in the online version, at https://doi.org/10.1016/j.jbiomech.2019.109370.

References

Amador, C., Urban, M., Kinnick, R., Chen, S., Greenleaf, J.F., 2013. In vivo swine kidney viscoelasticity during acute gradual decrease in renal blood flow: pilot study. Revista ingenieria biomedica 7, 68–78.
Amador, C., Urban, M.W., Greenleaf, J.F., Warner, L.V., 2009. Measurements of swine renal cortex shear elasticity and viscosity with Shearwave Dispersion Ultrasound Vibrometry (SDUV). 2009 IEEE International Ultrasonics Symposium, 491–494.
Aristizabal, S., Carrascal, C.A., Nenadic, I.Z., Greenleaf, J.F., Urban, M.W., 2018. Application of acoustoelasticity to evaluate nonlinear modulus in ex vivo kidneys. IEEE Trans. Ultrason. Ferroelectr. Freq. Control 65, 188–200.
Babicz, M., Kropiwiec-Domanska, K., Szyndler-Nędza, M., Grzebalska, A.M., Łuszczewska Sierakowska, I., Wawrzyniak, A., Hałabis, M., 2018. Physicochemical parameters of selected internal organs of fattening pigs and wild boars. Ann. Anim. Sci. 18, 575–591.
Barr, R.G., Nakashima, K., Amy, D., Cosgrove, D., Farrokh, A., Schafer, F., Bamber, J.C., Castera, L., Choi, B.I., Chou, Y.H., Dietrich, C.F., Ding, H., Ferraioli, G., Filice, C., Friedrich-Rust, M., Hall, T.J., Nightingale, K.R., Palmeri, M.L., Shiina, T., Suzuki, S., Sporea, I., Wilson, S., Kudo, M., 2015. Wfumb guidelines and recommendations for clinical use of ultrasound elastography: Part 2: Breast. Ultrasound Med. Biol. 41, 1148–1160.
Barr, R.G., Zhang, Z., 2012. Effects of precompression on elasticity imaging of the breast. J. Ultrasound Med. 31, 895–902.
Bernal, M., Chamming's, F., Couade, M., Bercoff, J., Tanter, M., Gennisson, J., 2016. In vivo quantification of the nonlinear shear modulus in breast lesions: Feasibility study. IEEE Trans. Ultrason. Ferroelectr. Freq. Control 63, 101–109.
Boyce, M.C., Arruda, E.M., 2001. Swelling and mechanical stretching of elastomeric materials. Math. Mech. Solids 6, 641–659.
Carlson, L.C., Romero, S.T., Palmeri, M.L., Muñoz del Rio, A., Esplin, S.M., Rotemberg, V.M., Hall, T.J., Feltovich, H., 2015. Changes in shear wave speed pre- and post-induction of labor: a feasibility study. Ultrasound Obstet. Gynecol. 46, 93–98.
Chatzistergos, P.E., Behforootan, S., Allan, D., Naemi, R., Chockalingam, N., 2018. Shear wave elastography can assess the in-vivo nonlinear mechanical behavior of heel-pad. J. Biomech. 80, 144–150.
Chung, S.H., Cerussi, A.E., Klifa, C., Baek, H.M., Birgul, O., Gulsen, G., Merritt, S.I., Hsiang, D., Tromberg, B.J., 2008. In vivowater state measurements in breast cancer using broadband diffuse optical spectroscopy. Phys. Med. Biol. 53, 6713–6727.
Correas, J.M., Tissier, A.M., Khairoune, A., Vassiliu, V., Méjean, A., Hélénon, O., Memo, R., Barr, R.G., 2015. Prostate cancer: diagnostic performance of real-time shear-wave elastography. Radiology 275, 280–289.
DeWall, R.J., Jiang, J., Wilson, J.J., Lee, K.S., 2014. Visualizing tendon elasticity in an ex vivo partial tear model. Ultrasound Med. Biol. 40, 158–167.
Dobrynin, A.V., Carrillo, J.M.Y., 2011. Universality in nonlinear elasticity of biological and polymeric networks and gels. Macromolecules 44, 140–146.
Dobrynin, A.V., Carrillo, J.M.Y., Rubinstein, M., 2010. Chains are more flexible under tension. Macromolecules 43, 9181–9190.
Evers, D.J., Hendriks, B.H.W., Lucassen, G.W., van der Voort, M., 2011. Diagnosis of breast cancer using diffuse optical spectroscopy from 500 to 1600 nm: comparison of classification methods. J. Biomed. optics, 16.
Fischer, H., Polikarpov, I., Craievich, A.F., 2004. Average protein density is a molecular-weight-dependent function. Protein Sci.: Publ. Protein Soc. 13, 2825–2828.
Gennisson, J.L., Grenier, N., Combe, C., Tanter, M., 2012. Supersonic shear wave elastography of in vivo pig kidney: influence of blood pressure, urinary pressure and tissue anisotropy. Ultras. Med. Biol. 38, 1559–1567. https://doi.org/10.1016/j.ultrasmedbio.2012.04.013.
Gennisson, J.L., Renier, M., Catheline, S., Barriere, C., Bercoff, J., Tanter, M., Fink, M., 2007. Acoustoelasticity in soft solids: assessment of the nonlinear shear modulus with the acoustic radiation force. J. Acoust. Soc. Am. 122, 3211–3219.
Goenezen, S., Dord, J., Sink, Z., Barbone, P.E., Jiang, J., Hall, T.J., Oberai, A.A., 2012. Linear and nonlinear elastic modulus imaging: an application to breast cancer diagnosis. IEEE Trans. Med. Imaging 31, 1628–1637.
Grasland-Mongrain, P., Zorgani, A., Nakagawa, S., Bernard, S., Paim, L.G., Fitzharris, G., Catheline, S., Cloutier, G., 2018. Ultrafast imaging of cell elasticity with optical microelastography. Proc. Nat. Acad. Sci. 115, 861–866.
Haddadin, I.S., McIntosh, A., Meisamy, S., Corum, C., Snyder, A.L.S., Powell, N.J., Nelson, M.T., Yee, D., Garwood, M., Bolan, P.J., 2009. Metabolite quantification and high-field mrs in breast cancer. NMR Biomed. 22, 65–76.
Hall, T.J., Barbone, P., Oberai, A.A., Jiang, J., Dord, J.F., Goenezen, S., Fisher, T.G., 2011. Recent results in nonlinear strain and modulus imaging. Curr. Med. Imaging Rev. 7, 313–327.
Helfenstein, C., Gennisson, J.L., Tanter, M., Beillas, P., 2015. Effects of pressure on the shear modulus, mass and thickness of the perfused porcine kidney. J. Biomech. 48, 30–37.
Humphrey, J., 2003. Review paper: continuum biomechanics of soft biological tissues. Proc. Roy. Soc. Lond. A: Math. Phys. Eng. Sci. 459, 3–46.
Jiang, Y., Li, G., Qian, L.X., Liang, S., Destrade, M., Cao, Y., 2015. Measuring the linear and nonlinear elastic properties of brain tissue with shear waves and inverse analysis. Biomech. Model. Mechanobiol. 14, 1119–1128.
Jiang, Y., Li, G.Y., Qian, L.X., Hu, X.D., Liu, D., Liang, S., Cao, Y., 2015. Characterization of the nonlinear elastic properties of soft tissues using the supersonic shear imaging (SSI) technique: Inverse method, ex vivo and in vivo experiments. Med. Image Anal. 20, 97–111.
Larin, K.V., Sampson, D.D., 2017. Optical coherence elastography: OCT at work in tissue biomechanics. Biomed. Opt. Express 8, 1172–1202.
Latorre-Ossa, H., Gennisson, J., De Brosses, E., Tanter, M., 2012. Quantitative imaging of nonlinear shear modulus by combining static elastography and shear wave elastography. IEEE Trans. Ultrason. Ferroelectr. Freq. Control 59, 833–839.
Liu, T., Hall, T.J., Barbone, P.E., Oberai, A.A., 2017. Inferring spatial variations of microstructural properties from macroscopic mechanical response. Biomech. Model. Mechanobiol. 16, 479–496.
Liu, Z., Toh, W., Ng, T.Y., 2015. Advances in mechanics of soft materials: a review of large deformation behavior of hydrogels. Int. J. Appl. Mech. 07, 1530001.
Mariappan, Y.K., Glaser, K.J., Ehman, R.L., 2010. Magnetic resonance elastography: a review. Clin. Anat. 23, 497–511.
Nazari, N., Barbone, P., 2018. Shear wave speed in pressurized soft tissue. J. Mech. Phys. Solids 119, 60–72.
Nightingale, K.R., Rouze, N.C., Rosenzweig, S.J., Wang, M.H., Abdelmalek, M.F., Guy, C.D., Palmeri, M.L., 2015. Derivation and analysis of viscoelastic properties in human liver: impact of frequency on fibrosis and steatosis staging. IEEE Trans. Ultrason. Ferroelectr. Freq. Control 62, 165–175.
Ogden, R.W., 2007. Incremental statics and dynamics of pre-stressed elastic materials. In: Destrade, M., Saccomandi, G. (Eds.), Waves in Nonlinear Pre-Stressed Materials. Springer, pp. 1–27. book section 1.
Parker, K.J., 2014. A microchannel flow model for soft tissue elasticity. Phys. Med. Biol. 59, 4443–4457.
Parker, K.J., Ormachea, J., McAleavey, S.A., Wood, R.W., Carroll-Nellenback, J.J., Miller, R.K., 2016. Shear wave dispersion behaviors of soft, vascularized tissues from the microchannel flow model. Phys. Med. Biol. 61, 4890–4903.
Rosen, D., Jiang, J., 2018. Fourier-domain shift matching: a robust time-of-flight approach for shear wave speed estimation. IEEE Trans. Ultrason. Ferroelectr. Freq. Control 65, 729–740.

Rosen, D.P., Jiang, J., 2019. A comparison of hyperelastic constitutive models applicable to shear wave elastography (SWE) data in tissue-mimicking materials. Phys. Med. Biol. 64. 055014.
Rotemberg, V., Palmeri, M., Nightingale, R., Rouze, N., Nightingale, K., 2011. The impact of hepatic pressurization on liver shear wave speed estimates in constrained versus unconstrained conditions. Phys. Med. Biol. 57, 329–341.
Shah, N., Hsiang, D., Durkin, A., Butler, J., 2006. In vivo absorption, scattering, and physiologic properties of 58 malignant breast tumors determined by broadband diffuse optical spectroscopy. J. Biomed. optics, 11.
Shiina, T., Nightingale, K.R., Palmeri, M.L., Hall, T.J., Bamber, J.C., Barr, R.G., Castera, L., Choi, B.I., Chou, Y.H., Cosgrove, D., Dietrich, C.F., Ding, H., Amy, D., Farrokh, A., Ferraioli, G., Filice, C., Friedrich-Rust, M., Nakashima, K., Schafer, F., Sporea, I., Suzuki, S., Wilson, S., Kudo, M., 2015. WFUMB guidelines and recommendations for clinical use of ultrasound elastography: Part 1: Basic principles and terminology. Ultrasound Med. Biol 41, 1126–1147.
Singh, M., Han, Z., Li, J., Vantipalli, S., Aglyamov, S.R., Twa, M.D., Larin, K.V., 2018. Quantifying the effects of hydration on corneal stiffness with noncontact optical coherence elastography. J. Cataract Refractive Surgery 44, 1023–1031.
Tanter, M., Pernot, M., Gennisson, J.L., Fink, M., 2013. A review of the medical applications of shear wave elastography. J Acoust. Soc. Am. 134, 4009.
Ternifi, R., Gennisson, J.L., Tanter, M., Beillas, P., 2013. Effects of storage temperature on the mechanical properties of porcine kidney estimated using shear wave elastography. J. Mech. Behav. Biomed. Mater. 28, 86–93.
Vachutka, J., Sedlackova, Z., Furst, T., Herman, M., Herman, J., Salzman, R., Dolezal, L., 2018. Evaluation of the effect of tissue compression on the results of shear wave elastography measurements. Ultrason. Imaging 40, 380–393.
Warner, L., Yin, M., Glaser, K.J., Woollard, J.A., Carrascal, C.A., Korsmo, M.J., Crane, J. A., Ehman, R.L., Lerman, L.O., 2011. Noninvasive in vivo assessment of renal tissue elasticity during graded renal ischemia using mr elastography. Invest. Radiol. 46, 509–514.
Woodard, H.Q., White, D.R., 1986. The composition of body tissues. Brit. J. Radiol. 59, 1209–1218.